JOURNAL OF GEOPHYSICAL RESEARCH, VOL. 100, NO. B8, PAGES 15,101–15,116, AUGUST 10, 1995

A seismic reflection profile across the Cascadia subduction zone offshore central Oregon: New constraints on methane distribution and crustal structure

Anne M. Tréhu, Guibiao Lin, Edward Maxwell, and Chris Goldfinger
College of Oceanic and Atmospheric Sciences, Oregon State University, Corvallis

Abstract. In 1989, we conducted an onshore/offshore seismic experiment to image the crustal structure of the Cascadia forearc. In this paper, we discuss the processing and interpretation of a multichannel seismic reflection profile across the continental margin that was collected as part of this effort. This profile reveals several features of the forearc that were not apparent in an earlier, coincident reflection profile. One of the most important of these features is a very strong bottom simulating reflection (BSR) beneath the midslope region that is nearly continuous from water depths of about 1500 m to 600 m, where it appears to crop out on the seafloor. The pressure and temperature conditions at the BSR derived from our observations are remarkably consistent with the experimentally determined phase diagram for a methane hydrate/seawater system over a broad range of temperatures and pressures, assuming hydrostatic pressure and the temperature gradiant measured near the base of the continental slope during Ocean Drilling Program (ODP) leg 146. Interval velocities and reflection coefficients derived from the data indicate that the BSR represents a contrast between sediment with a small amount of hydrate overlying sediment containing free gas, consistent with results obtained during leg 146. Although the regional distribution of the anomalously strong BSR beneath the midslope is poorly known, we speculate that it may be related to apparent slope instability. The data also provide constraints on the thickness and geometry of the Siletz terrane, which is the basement beneath the shelf and acts as the subduction zone backstop. A deep reflection, which might mistakenly be interpreted to be Moho if coincident large-aperture data were not available, is interpreted to be the base of the Siletz terrane. A "recently" active strike-slip (?) fault zone that overlies the seaward edge of the Siletz terrane suggests that the Siletz terrane controls the location of decoupling of the subduction complex from the rest of the forearc.

Introduction

The Cascadia subduction zone has received considerable attention recently, both because of a large uncertainty about the seismic hazard it poses to the inhabitants of the Pacific Northwest region [e.g., *Heaton and Hartzell*, 1987; *Atwater*, 1987; *Grant et al.*, 1989; *Shedlock and Weaver*, 1991] and as a laboratory to study the effects of fluid flow in accretionary environments [e.g., *Kulm et al.*, 1986; *Moore et al.*, 1990, 1991; *Davis et al.*, 1990]. The data presented here provide constraints on the deep crustal structure, which are needed to evaluate the seismic hazard, and on the distribution of methane and thermal gradients within the suduction complex.

Snavely [1987] and *Snavely et al.* [1980] comprehensively summarize the available information about the geologic history and crustal structure of the continental margins of Oregon and Washington prior to recent acquisition of new data. Stratigraphic relationships demonstrate that the early Eocene-aged oceanic crustal rocks of the Siletz terrane, which forms the basement of the Oregon continental shelf as well as of the Oregon and southern Washington Coast Ranges, were sutured to North America approximately 50 m.y. ago. Overlying this terrane are sedimentary basins up to 7 km thick that contain many folds, unconformities and intrusions, reflecting episodic convergence and forearc volcanism. Seaward of the Siletz terrane is a well-developed accretionary prism that has formed since convergence was initiated seaward of the Siletz terrane during the late Eocene.

Recent offshore bathymetric, side scan sonar and seismic reflection data provide a clear image of the subduction zone deformation front. Those data indicate significant along-strike variation in structural style as the dominant mode of deformation changes from seaward verging thrust faulting south of 44°52'N to landward verging thrust faulting north of 44°52'N [*MacKay et al.*, 1992]. The transition occurs where the deformation front is cut by a northwest trending left-lateral strike-slip fault that extends from the abyssal plain seaward of the deformation front to the continental shelf (fault B of *Goldfinger et al.*, [1992], now known as the Daisy Bank fault). This fault represents one of a series of such faults that cut across the deformation front and accretionary prism [*Applegate et al.*, 1992; *Goldfinger et al.*, 1992] and may represent conduits for fluid flow within the prism [*Tobin et al.*, 1993].

In 1989, we conducted an onshore/offshore large-aperture crustal imaging experiment across the Cascadia subduction zone offshore central Oregon to obtain constraints on the velocity structure of the forearc (Figure 1). The western end of the profile is within a dense grid of high-resolution seismic reflection profiles [*MacKay et al.*, 1992] that was shot as a site survey for Ocean Drilling Program (ODP) leg 146 (Figure 1). Drilling was undertaken in September 1992, and was focused on examining fluid expulsion within the deformation front. On the continental

Paper number 95JB00240.
0148-0227/95/95JB-00240$05.00

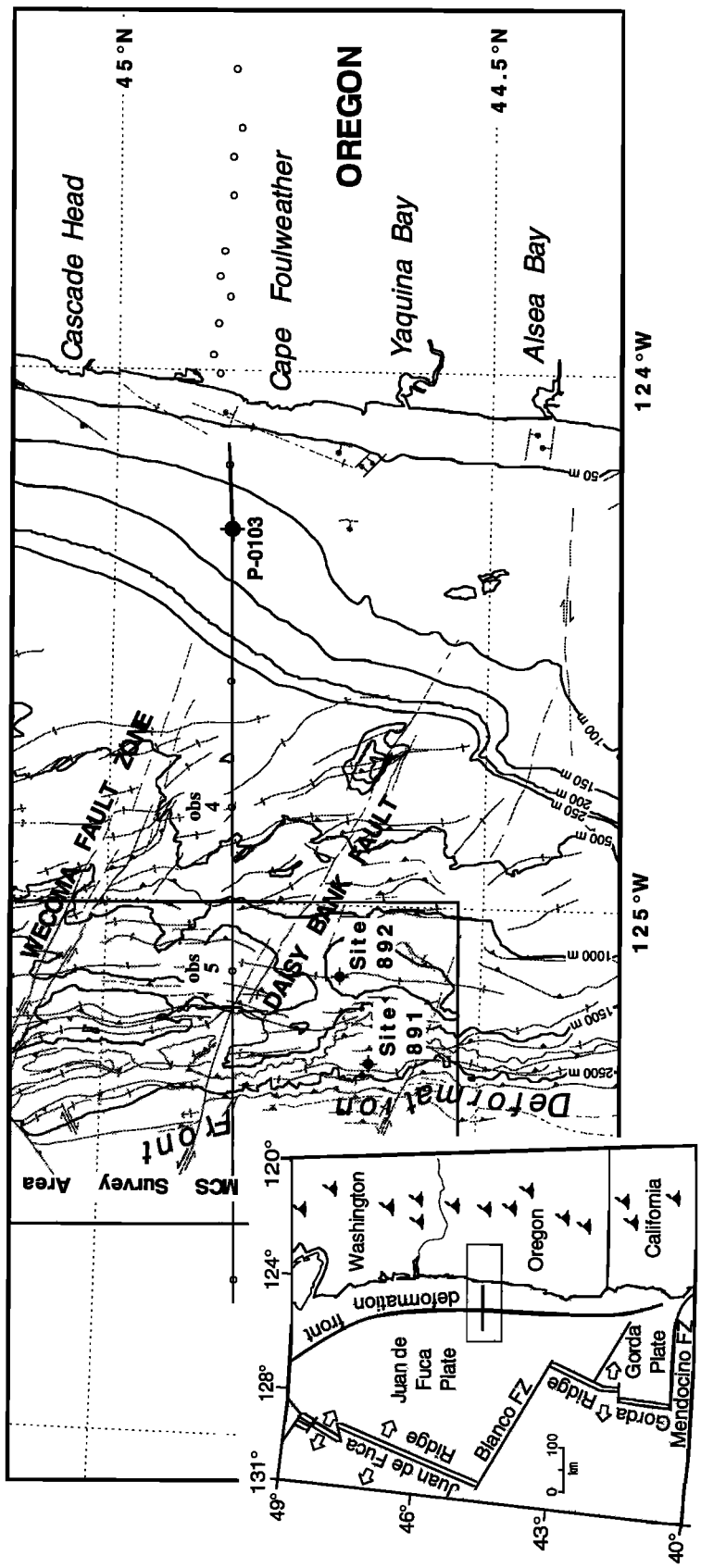

Figure 1. Map of the Oregon continental margin showing the location of the multichannel seismic-reflection profile (solid line) and of seismographs simultaneously recording large aperture data (open circles). Bathymetry, major faults and folds of the margin (from *MacKay et al.* [1992], and *Goldfinger et al.* [1992]), the location of the high-resolution ODP site survey (shaded box), recent ODP drill holes (sites 891 and 892), and an industry test well (P-0103) are also shown. The insert shows the plate tectonic setting of the profile.

shelf, the age and composition of the sediments and intrusive rocks overlying the Siletz basement are constrained by a deep industry test hole located along the profile [*Snavely*, 1987].

For the profile discussed in this paper, a tuned airgun array with a total volume of 128 L (7800 in^3) was deployed from the R/V *Geotide*, operated by DIGICON, and was fired at 30-s intervals. These shots were recorded by six ocean bottom and 10 onshore seismometers as well as by the 3833-m-long, 144-channel hydrophone cable towed by the R/V *Geotide*. In this paper, we present the multichannel seismic (MCS) reflection profile acquired by the R/V *Geotide*. The large-aperture data collected by the ocean bottom and onshore seismometers have been presented elsewhere [*Tréhu and Nakamura*, 1993; *Brocher et al.*, 1993]. The velocity model derived from the large-aperture data [*Tréhu et al.*, 1994; also A.M. Tréhu, manuscript in preparation, 1995] is used to help constrain interpretation of the reflection profile.

The new MCS profile presented here was shot coincident with an existing MCS profile acquired by the U.S. Geological Survey (USGS) in 1974 (profile OR-5 [Snavely, 1987]). Many features of the new profile are similar to features observed on the USGS profile, and we refer the reader to *Snavely* [1987] for a detailed discussion of that profile. In this paper, we concentrate on several features of the new data that are not apparent in the USGS profile. The most important of these features are an anomalously strong bottom simulating reflection (BSR) associated with the presence of gas hydrate beneath the continental slope, a shallow fault overlying the seaward edge of the Siletz terrane, and a deep reflection underlying the Siletz terrane. These features are probably observable in the new data but not in the older USGS data because of the greater bandwidth and strength of the seismic source in our experiment.

Data Processing

Sixteen seconds of data were collected at a sampling rate of 4 ms. The data were then sorted and binned into common midpoints (CMPs) spaced 12.5 m apart. Because the shot interval was 30 s (resulting in a shot spacing of 66±8 m), the fold of the data varies between 27 and 28, and trace spacing within CMPs averages 66 m. Shooting on time rather than distance was necessary in order to maximize the amount of data that could be recorded by ocean bottom seismometers (OBSs) with a recording capacity of 5 MBytes, and represents a compromise between the MCS and large-aperture objectives of the experiment. Fortunately such compromises should not be necessary in the future, as the storage capacity of OBSs has increased by orders of magnitude in the past few years.

Velocity analysis was conducted on every 50th CMP by manually picking the peaks on plots of semblance (an estimate of signal coherence between traces [*Sheriff and Geldart*, 1982]) as a function of velocity and time. For data seaward of the midslope region (CMP6500), velocities obtained by *Cochran et al.* [1994] were used. Not surprisingly, velocities are well defined in regions with numerous strong reflections; in regions with few reflections, velocities are poorly defined, and stacking velocities were estimated based on the OBS data. These velocities were then used to produce a preliminary stacked seismic section.

To constrain the nature of faint deep reflections observed in the preliminary stacked section, the data were resorted into 50-m bins, yielding 108-fold data with an average trace spacing of 33 m within each CMP gather. Several examples from the region from which deep reflections are observed are shown in Figure 2,

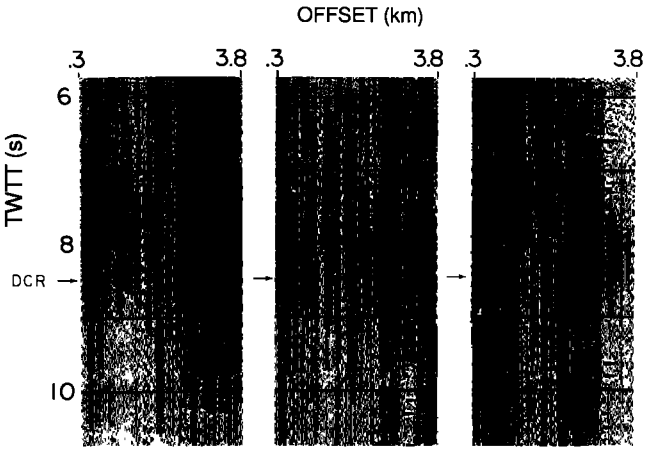

Figure 2. Examples of resorted, unstacked CMP gathers prior to application of automatic editing based on a specified threshold for the rms amplitude of the signal in the last 6 s of the recorded data. A series of very faint, but distinct, reflections (DCR) at 8–8.5 s twtt is indicated by arrows. These events are interpreted to be primary events from the lower crust because of the very small moveout, in contrast to the event at 6-s twtt, which may be a multiple of the basement reflection. CMPs 1075–1079, 1100–1104, and 1125–1129 are shown.

plotted with only an approximate spherical divergence correction applied to the amplitudes and no normal moveout correction. Reflections at 6- to 7-s two-way travel time (twtt) require a moveout similar to that of the basement arrival at 3-s twtt, suggesting that they may be multiples of the basement reflection. The arrival time of these reflections is also consistent with this interpretation. Faint reflections at 8.5- to 9-s twtt, on the other hand, show no measurable moveout, implying high seismic velocities and suggesting that they are primary events from the lower crust or Moho.

Figure 2 also shows that the amplitude of the background noise varies considerably from trace to trace and that the noise level exceeds the amplitude of the reflections at 8.5- to 9-s twtt on approximately one third of the traces. The noisy channels vary from shot to shot, complicating the editing process. We therefore designed an algorithm to automatically zero all traces that have an average amplitude in the lower 6 s of data falling above an empirically determined threshold. The amplitudes of the remaining traces were then scaled to compensate for the reduced fold. This processing technique was quite successful in improving the signal-to-noise ratio of data from the lower crust (Figure 3).

The data (sorted into 12.5-m bins of 27- to 28-fold data) were then stacked and migrated using a 45° finite difference algorithm and a velocity model derived from the stacking velocities. The data were band-pass filtered with a passband of 5 to 25 Hz above 3-s twtt and a passband of 5 to 20 Hz below 3.5-s twtt, and four adjacent traces were stacked together for this display. Amplitudes were scaled by a factor of (travel time)$^{2.5}$ to approximately correct for spherical divergence. The migrated data for the entire profile are shown in Figure 4a. Amplitudes in the eastern half of the profile (lower panel) have been increased by a factor of 2 compared to amplitudes in the western half (upper panel). The annotated profile is shown in Figure 4b. Contours from the velocity model obtained from the large-aperture data [*Tréhu et al.*, 1994] are shown in Figure 4c. The same velocity model and coincident potential field anomalies are shown as a function of depth in Figure 4d.

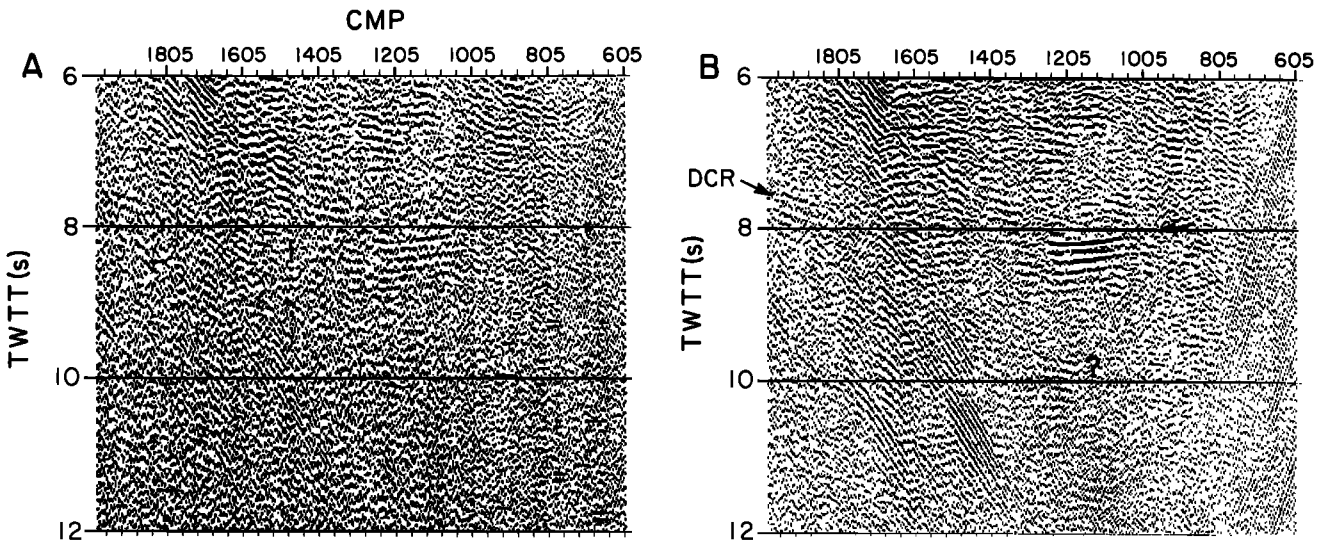

Figure 3. Unmigrated, stacked seismic reflection section showing the deep reflections (DCR) beneath the continental shelf (a) before application of automatic trace editing and (b) after application of automatic trace editing.

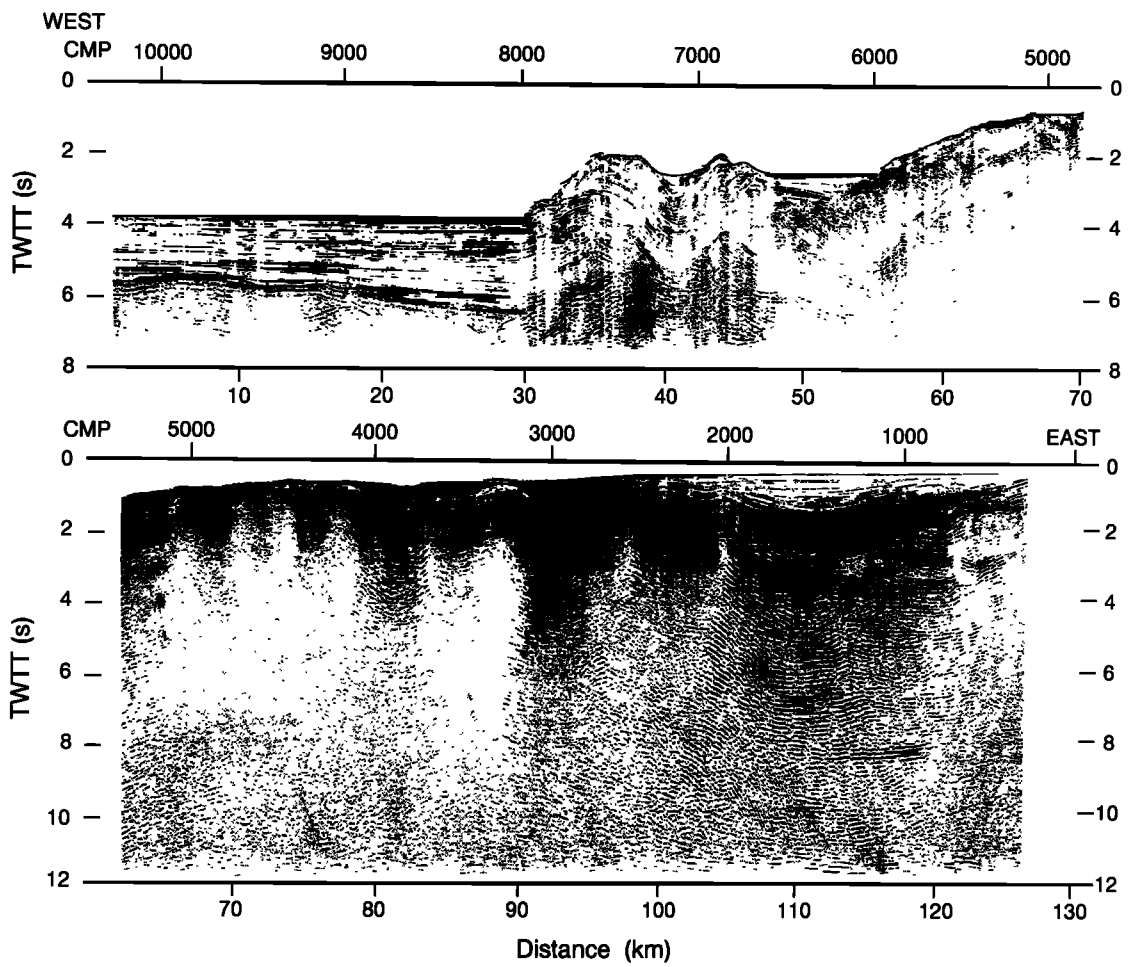

Figure 4a. Finite difference migrated stacked seismic section. A band-pass filter with a passband of 5–25 Hz above 3-s twtt and 5–20 Hz below 3.5-s twtt was applied, and four adjacent traces were stacked together for this display. Amplitudes are scaled by a factor of (travel time)$^{2.5}$. Amplitudes in the eastern half of the profile (lower panel) have been increased by a factor of 2 compared to amplitudes in the western half (upper panel). See text for further description of processing procedure.

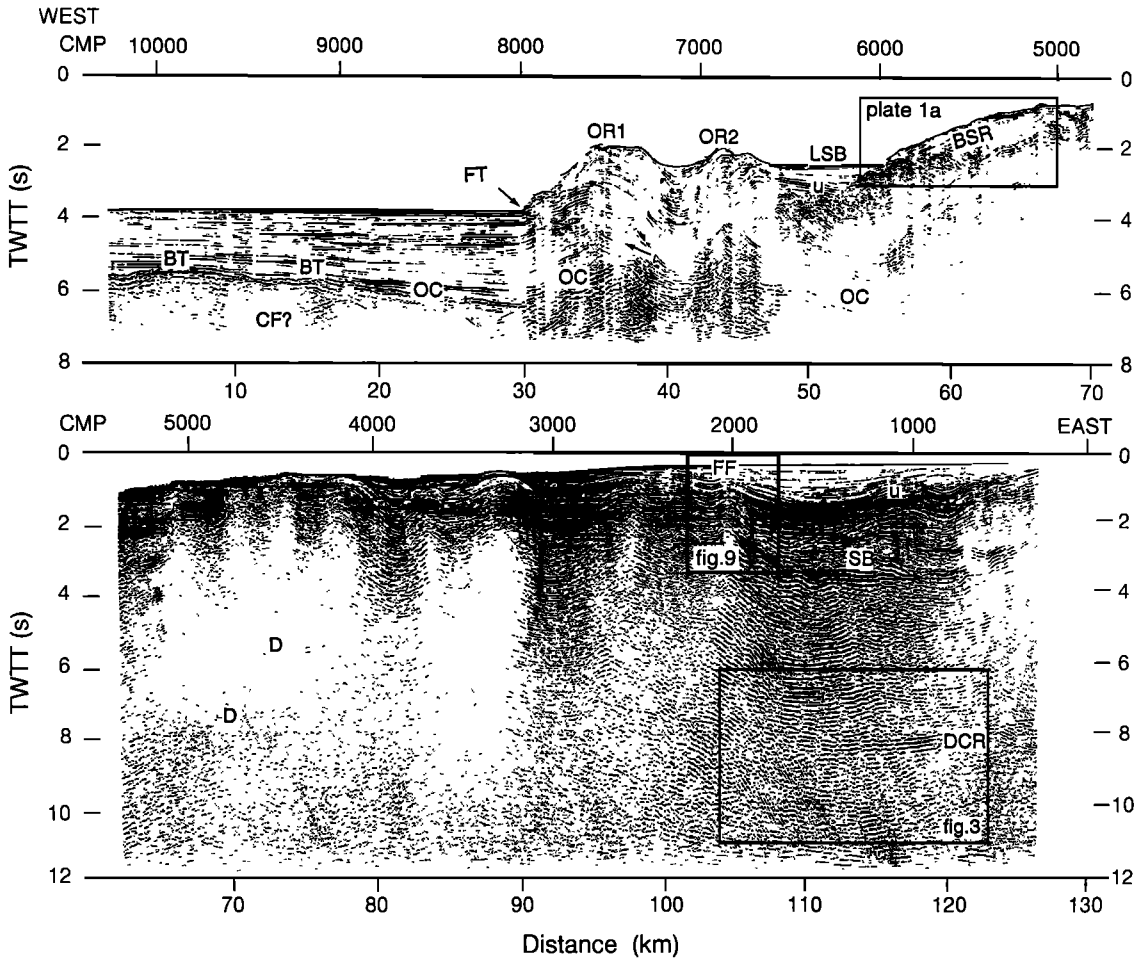

Figure 4b. Annotated seismic section. BSR, bottom simulating reflections; BT, basement topography; CF, crustal fault; D, diffraction from topography or shallow structure; DCR, deep crustal reflection; FF, Fulmar fault; FT, frontal thrust; LSB, lower slope basin; OC, top of oceanic crust; OR, outer ridge; SB, Siletz basement; u, unconformity.

Discussion

The Deformation Front

Proceeding from the abyssal plain to the continental shelf, we now discuss the major features of this profile. The sediments of the abyssal plain are flat lying, with a slight thickening observed as the deformation front is approached. Although few faults are observed in the abyssal plain sediments on this profile, many of the seismic profiles in the high-resolution ODP site-survey data show small thrust faults in the abyssal plain sediments, representing a protodeformation front [*MacKay et al.*, 1992].

The top of oceanic crust is well imaged beneath the abyssal plain. Note the presence of significant topography on the oceanic crust near km 2–9 and km 12–18 (BT on Figure 4b). That the sediments lap onto the sides of these basement hills suggests that the topography represents constructional volcanic features formed at or near the spreading center. Using a sediment velocity of 3 km/s derived from the OBS data, we calculate a height of about 450 m for these hills. There is also tentative evidence for faulting within the oceanic crust (labeled CF). Additional data are needed to determine the three-dimensional configuration of the basement topography and intracrustal deformation, but the presence of these features is mentioned because it suggests that some of the tectonic complexity within the young accretionary prism may be due to topography on the subducted oceanic crust.

A clear seaward verging fault (FT on Figure 4b) is observed at the deformation front. Although this profile was located very close to the transition from a narrow seaward verging deformation front to a broad landward verging deformation front [*MacKay et al.*, 1992], it shows structures characteristic of a seaward verging deformation front, with the frontal thrust clearly visible. Projecting the frontal thrust onto the velocity model indicates that it dips approximately 30° to the east and that it comes within 1–2 km of the top of the subducting oceanic crust. The data quality on this profile is not adequate to determine whether all sediment on the subducting plate is being accreted or whether the primary subduction decollement is located within the sedimentary column. Based on the high-resolution site-survey data, however, *MacKay et al.* [1992] have estimated that the decollement is approximately 1.4 km above the oceanic crust in this part of the subduction zone.

Two outer ridges (OR1, OR2) and a relatively large lower slope basin (labeled LSB) are observed immediately landward of the deformation front (Figure 4b). The lower slope basin records an episode of relatively rapid uplift, which is recorded as an unconformity (u on Figure 4b), as well as gradual continuous

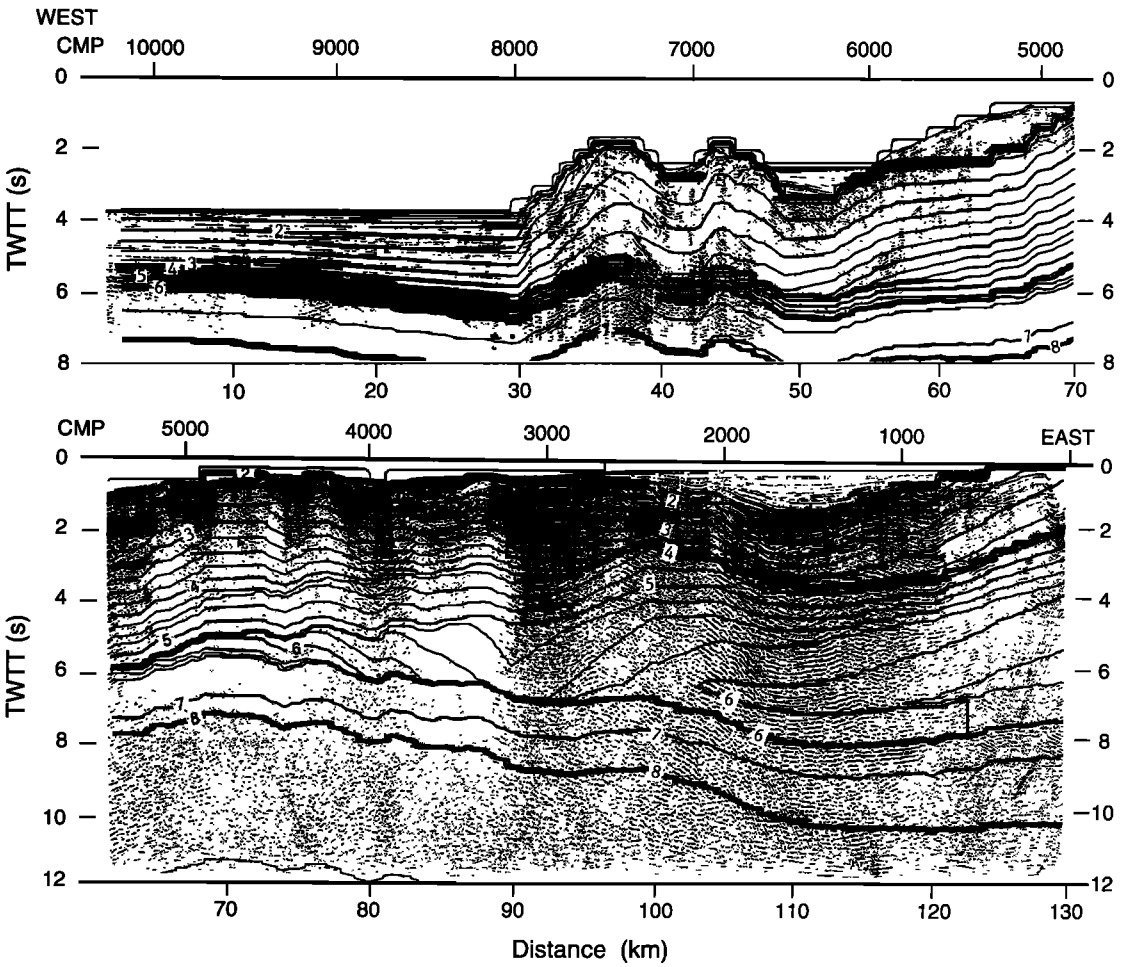

Figure 4c. Velocity contours obtained from inversion of travel times of the large aperture data overlain on the MCS profile.

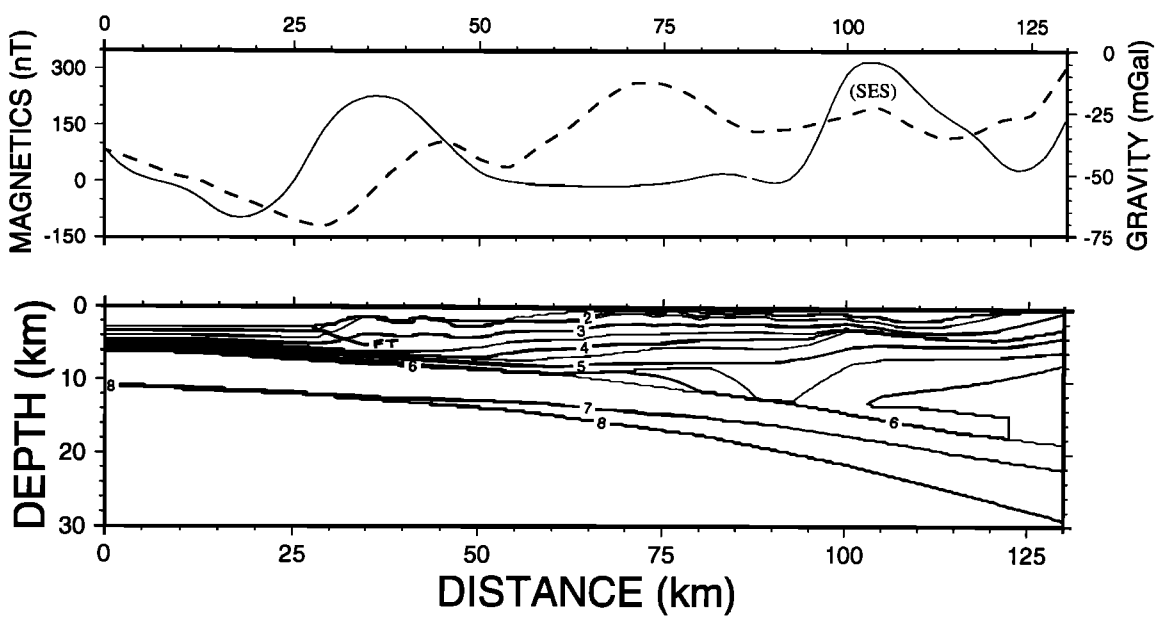

Figure 4d. Velocity model shown as a function of depth with no vertical exaggeration. Magnetic (solid line) and free-air gravity (dashed line) anomalies are also shown. The seaward edge of the Siletz terrane (SES) is evident in the magnetic and gravity anomalies.

uplift [*Snavely*, 1987]. The timing of the uplift event is not constrained by these data, but probably reflects a period of sedimentary underplating beneath the basin.

The large-aperture data indicate higher velocities beneath the outer ridges (Figure 4c) than are found in the abyssal plain sediments [*Tréhu et al.*, 1994], suggesting sediment compaction and dewatering during accretion to the upper plate. At first sight, this result appears to disagree with the relative velocity decrease in this region reported by *Lewis* [1992] and *Cochrane et al.* [1994] and interpreted to indicate an increase in porosity due to deformation of the sediments landward of the deformation front. These results, however, can be reconciled by considering that the measurements of *Lewis* [1992] and *Cochrane et al.* [1994] were primarily sensitive to the upper 2 km of the accretionary prism. The apparent discrepancy between their model and ours may be due to poor resolution of the velocity gradient in the uppermost sediments in our model and limited offsets recorded by *Lewis* [1992] and *Cochrane et al.* [1994]. Figure 5 shows two velocity models that fit the travel time data for OBSs 4 and 5 (Figure 1) equally well, within the resolution of the data, and indicates that if the velocity within the ridges just landward of the deformation front decreases, then the velocity deeper within the accretionary prism must increase abruptly to match the arrival times observed in our data.

The Subducted Oceanic Crust

The top of oceanic crust can be traced for approximately 30 km east of the deformation front. Because of the complexity of the overlying structure, the image of this surface is discontinuous and the detailed structure of the subducted oceanic crust cannot be resolved. This reflection was useful, however, for helping to constrain the position of the top of the oceanic crust in a model of the velocity structure of the margin obtained from travel time inversion of large-aperture data [*Tréhu et al.*, 1994].

No coherent reflections are observed from the subducted oceanic crust of the Juan de Fuca plate beneath the middle and upper continental slope, in spite of our careful attempts to increase the signal-to-noise ratio through the procedure described above. In fact, very little seismic energy is returned from greater than 1 s after the seafloor reflection, and the only coherent events observable in this region are diffractions from topographic features out of the plane of the profile (labeled D in Figure 4b). Wide-angle reflections from the base of the crust observed in the large aperture data, however, confirm that oceanic crust of the subducted Juan de Fuca plate underlies this region.

The BSR

A strong reflection is observed approximately 0.3 s beneath the seafloor near CMP 5900 and shallows gradually until it appears to outcrop at the seafloor near CMP 5100 (Figure 4 and Plate 1a). This reflection is similar to reflections observed on many continental margins and known for some time to be related the presence of methane hydrate in the sediments [e.g., *Shipley et al.*, 1979]. These seismic events are generally referred to as BSRs (bottom simulating reflections) because they tend to be parallel to the seafloor. A strong BSR is widespread on the lower slope of the Oregon continental margin and was drilled approximately 17 km south of CMP 2500 during ODP leg 146 [*ODP Leg 146 Scientific Party*, 1993]. It was found to result from the presence of free methane gas below a layer with a small amount of methane hydrate, which produced a velocity decrease with depth from 1.75 km/s just above the BSR to 1.25 km/s below it. On the profile discussed here, BSR is a misnomer, as this event gradually shallows landward from about 270 m below the seafloor at a water depth of 1512 m until it appears to outcrop on the seafloor at a water depth of about 600 m.

Because of the wide range of water depths over which the BSR is observed (Plate 1b), these data provide an excellent opportunity to test how closely the observations follow the experimental phase diagram for the transition from methane hydrate to free gas. A number of parameters, including seafloor temperature, subsurface temperature gradient, and water and sediment velocity and density structure are needed to derive an apparent phase boundary from the BSR observations. In the absense of subsurface temperature measurements, several workers have assumed that the BSR observations follow the phase diagram and have used these observations to derive estimates of heat flow.

Seafloor temperature as a function of water depth was obtained from monthly averages of physical oceanographic measurements in an 0.5° square centered on 45°N, 125.5° W.

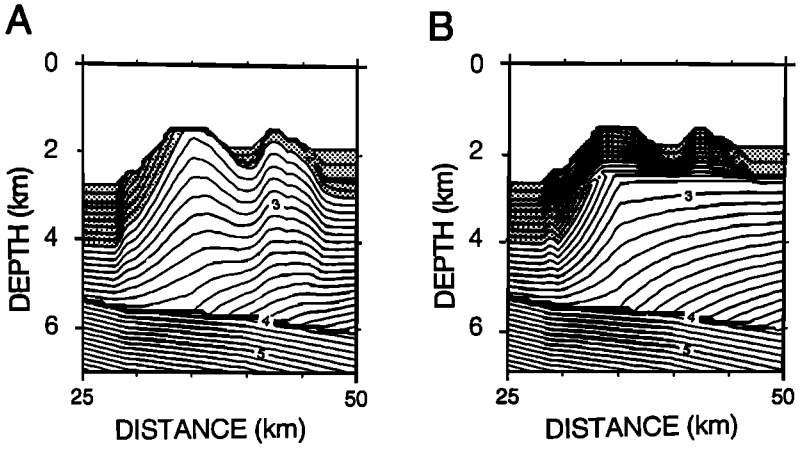

Figure 5. (a) Detail of the velocity model of Figure 4c in the region of the deformation front. (b) An alternative velocity model that also fits coincident ocean bottom seismometer data and is constrained to be consistent with the results of *Lewis* [1992] in the upper kilometer beneath the seafloor. Regions with velocity less than 2.5 km/s are shaded.

Water temperatures do not show significant annual variation below 100 m (Figure 6a) and can be precisely estimated by a simple function [seafloor temperature (°C) = 2.6 + A + B, where A = (1510 – water depth)0.002; B = 0 for water depth greater than 800 m; and B = (800 – water depth)0.0013 for water depth less than 800 m].

Travel times to the seafloor and to the BSR were digitized from the stacked and migrated record section and converted to depth. Velocities for the water and sediment were based on interval velocities obtained from detailed semblance analyses of the MCS data (Figure 7), which indicate water velocities of 1.485–1.5 km/s and velocities for the sediment lying between the seafloor and the BSR of 1.52–1.67 km/s, with velocity estimates increasing as the water and sediment thicknesses increase. While the interval velocity estimates may be biased by seafloor and BSR dips of up to 8° (3° in the region of anomalously large amplitude BSR), these results suggest low interval velocities above the BSR, indicating that relatively little hydrate is present. Figure 6b shows the water depth for assumed water velocities of 1.485 and 1.5 km/s (indistinguishable at the scale of the figure) and sediment thicknesses for velocities of 1.6 and 1.8 km/s. Assuming that the temperature gradient of 0.051 °K/m (as measured during leg 146 and reported by *ODP Leg 146 Scientific Party* [1993]) and a density of 1.0 g/cm^3 for water, we derive the temperature and hydrostatic pressure at the BSR shown in Figure 6c.

Additional considerations in deriving the pressure and temperature at the BSR from the seismic data concern whether the thermal gradient is constant and whether the pressure is hydrostatic or lithostatic. Several studies have used BSR observations combined with experimental observations of the hydrate/gas phase boundary to derive estimates of thermal gradient and consequently heat flow [e.g., *Shipley et al.*, 1979; *Yamano et al.*, 1982; *Davis et al.*, 1990; *Hyndman and Davis*, 1992; *Hyndman et al.*, 1993; *Zwart and Moore*, 1993]. Although most of those studies have assumed that pressure at the BSR is lithostatic, *Hyndman et al.* [1992] have argued that the hydrostatic pressure should be used for these calculations. To illustrate the effect of variations in the thermal gradient, we show pressure and temperature conditions at the BSR calculated for a range of temperature gradients assuming lithostatic pressure (Figure 6d, assuming a sediment density of 2.0 g/m^3) and hydrostatic pressure (Figure 6e). Water and sediment velocities of 1.5 and 1.8 km/s, respectively, were used in these calculations. These curves are compared to experimentally determined phase diagrams for methane

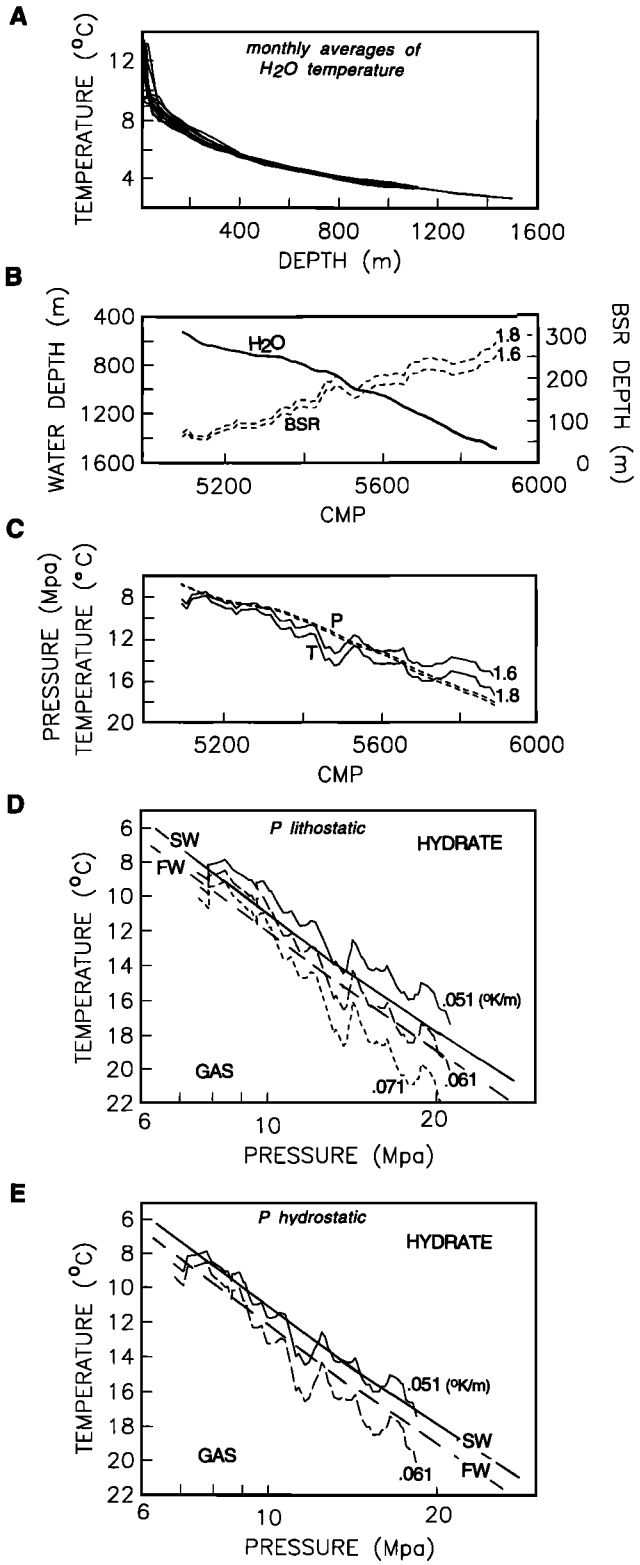

Figure 6. (Opposite) (a) Monthly averages of temperature within the water column obtained from physical oceanographic measurements (D. Pillsbury, personal communication, 1994). (b) Water depth and thickness of sediments overlying the BSR. Curves for water depth calculated assuming acoustic velocities in water of 1.490 and 1.50 km/s are identical at this scale. Further calculations were done assuming a water velocity of 1.5 km/s. Sediment thicknesses calculated assuming sediment velocities of 1.6 and 1.8 km/s are shown. (c) Pressure and temperature conditions at the BSR calculated assuming a thermal gradient of 0.051 °K/m, hydrostatic pressure, and sediment velocities of 1.6 and 1.8 km/s. (d) Derived pressure and temperature conditions at the BSR compared to experimentally determined pressure and temperature conditions for the methane gas/hydrate phase boundary in pure water and in a solution of water with 3.5% NaCl. Curves are shown assuming lithostatic pressure, sediment velocity and density of 1.8 km/s and 2.0 g/cm^3, respectively, and several temperature gradients. (e) Derived pressure and temperature conditions at the BSR compared to experimentally determined pressure and temperature conditions for the methane gas/hydrate phase boundary in pure water and in a solution of water with 3.5% NaCl. Curves are shown assuming hydrostatic pressure, sediment velocity and density of 1.8 km/s and 2.0 g/cm^3, respectively, and several temperature gradients.

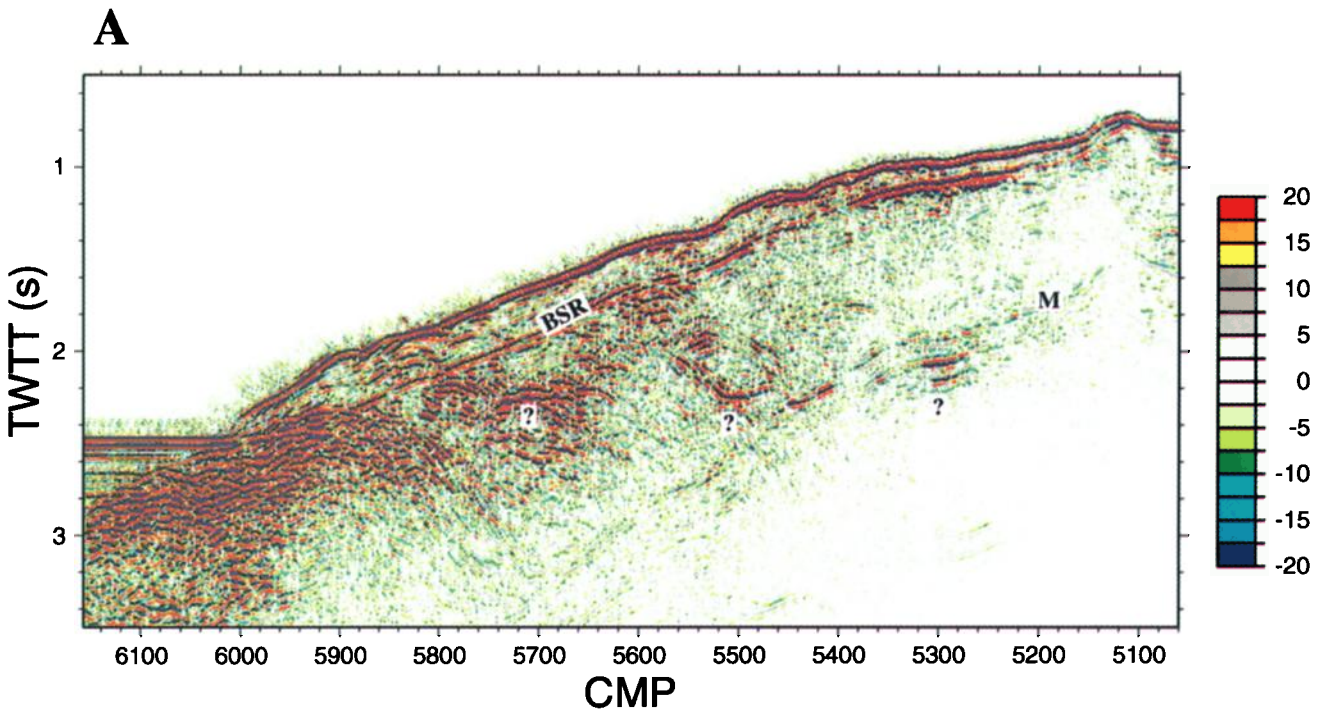

Plate 1a. Detail of the seismic section across the midslope region where a strong BSR is observed. Amplitudes have been scaled by a factor of (time)$^{1.5}$, and all traces are normalized to the same scale. The color-coded amplitude scale indicates relative amplitudes. The BSR and seafloor multiple (M) are labeled. Question marks indicate particularly bright reflections/diffractions from beneath the BSR. One hundred CMPs are equal to approximately 1250 m. Vertical exaggeration is approximately 3, assuming a velocity of 1500 m/s.

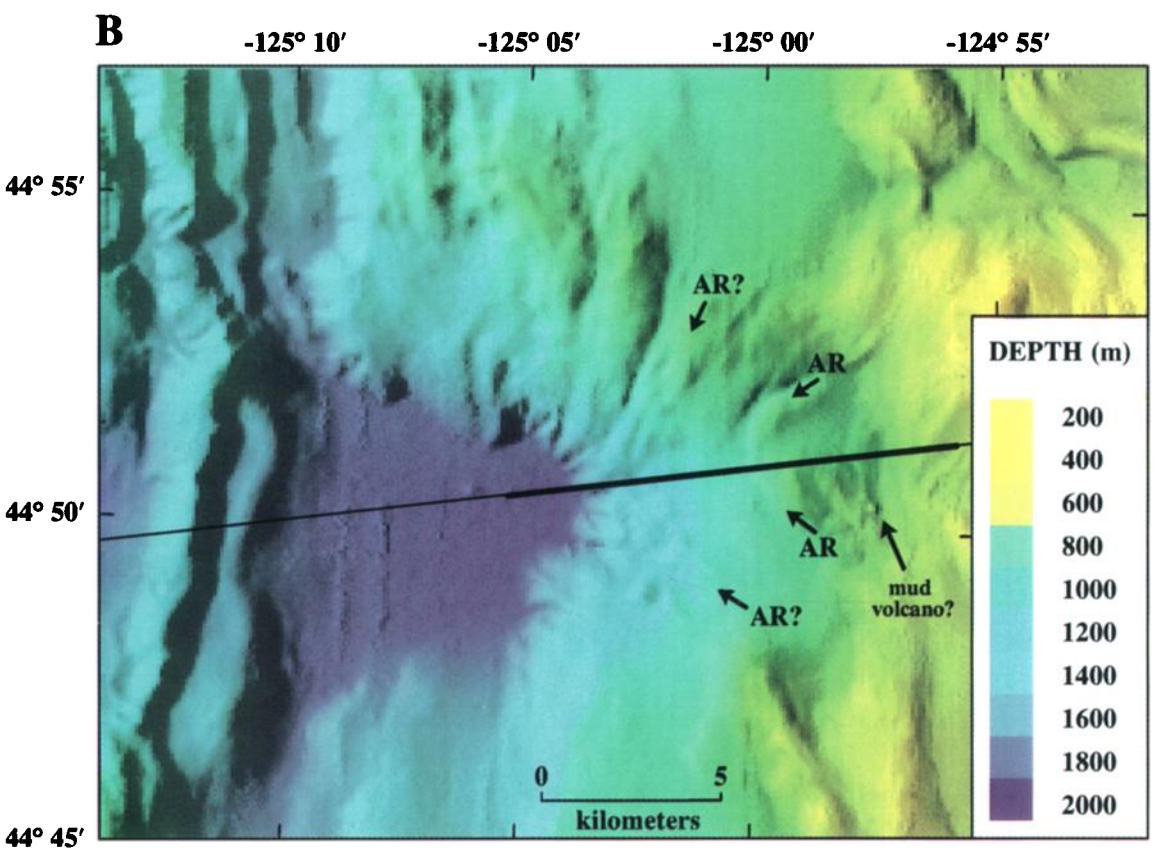

Plate 1b. Topography of the continental slope displayed as a color image with illumination from the west. Bathymetric data were collected and processed by NOAA staff at Pacific Marine Environmental Laboratory (PMEL), Newport, Oregon, and at Rockville, Maryland. Bold line shows the position of the seismic profile shown in Plate 1a. The arcuate ridges discussed in the text are indicated by "AR." A possible mud volcano near where the BSR outcrops on the seafloor is also indicated. Faint north-south trending "ridges" such as those near 44° 48', –125° 08' probably represent errors in the data.

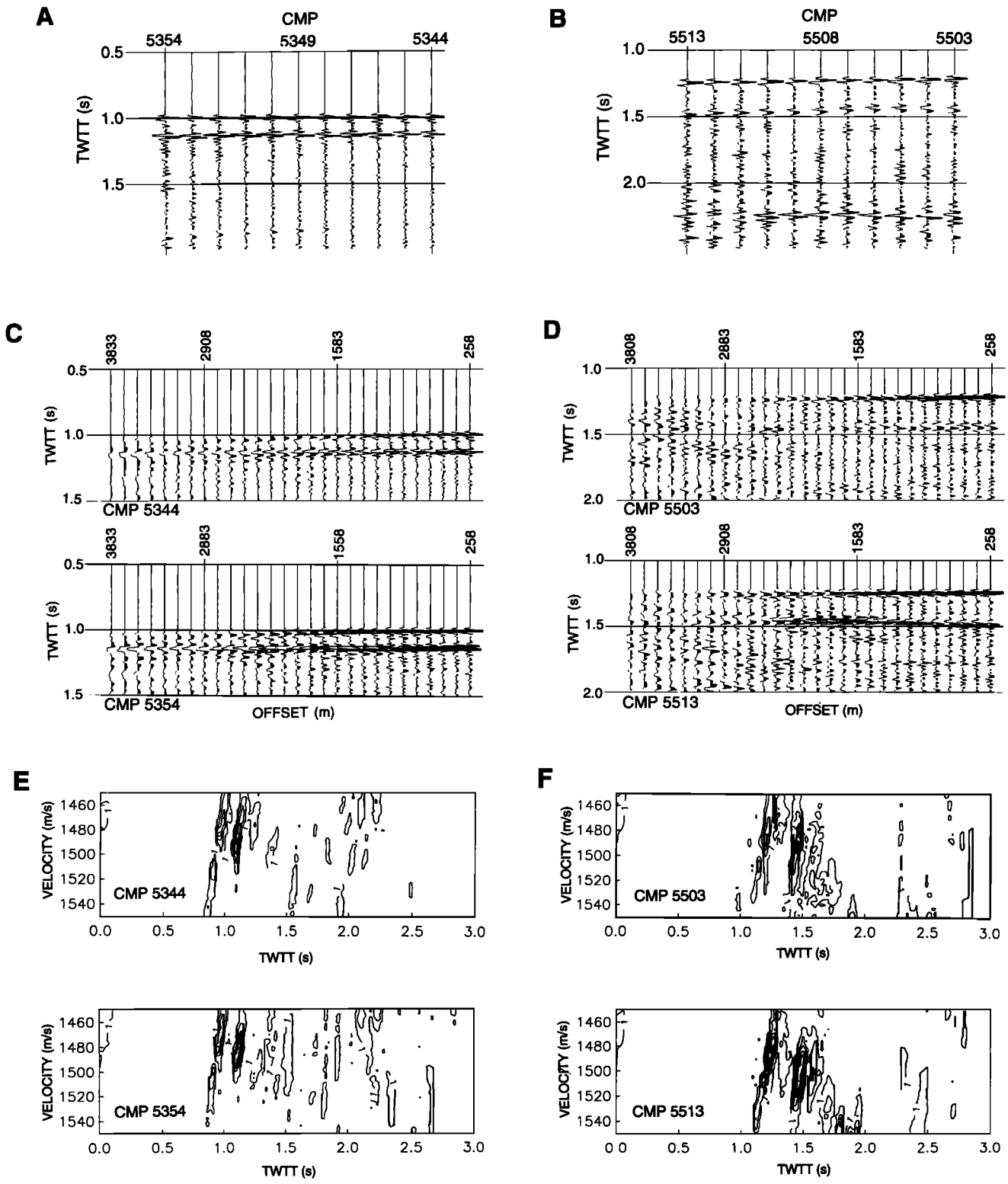

Figure 7. Examples of the BSR wavelet. Data have not been processed except for anti-alias filtering done prior to recording 4 ms and resampling to 8 ms and correction for normal moveout assuming a velocity of 1490 km/s. (a and b) Near trace of adjacent CMPs for two portions of the profile. The question mark on Figure 7b indicates a strong reflection/diffraction from a bright spot beneath the BSR. (c and d) CMP gathers corresponding to four of the traces shown in Figures 7a and 7b. Amplitudes have been approximately corrected for spherical divergence by a factor of time[1]. All traces are plotted at the same scale. At large offsets, as the seafloor and BSR reflections come together, the waveforms are distorted because of the normal moveout. Velocity analyses of the data in Figures 7c and 7d, displayed as contours of semblance as a function of velocity and time, are shown in Figures 7e and 7f, respectively.

in pure water and in a solution of water with 3.5% NaCl [*Hyndman et al.*, 1992; *Hyndman and Davis*, 1992].

Figure 6e shows that the observed shallowing of the BSR follows the expected phase relationship for methane hydrate stability remarkably well compared to observations in many other regions [e.g., *Shipley et al.*, 1979] for a constant thermal gradient of 0.051 °K/m, assuming hydrostatic pressure. Oscillations in the predicted stability curve are associated with small-scale seafloor topography that may result from landsliding, as discussed below. Most of these oscillations do not appear to correspond to faults that reach the seafloor and may reflect smoothing of the subsurface pressure and temperature fields due to the shear strength of the sediment and lateral heat conduction, respectively, rather than to upwelling of warm fluids along faults, as has been inferred near the deformation front [*Zwart and Moore*, 1993]. The largest amplitude oscillations, between CMPs 5417–5529 and upslope from CMP 5155, however, do appear to correspond to a fault and to an apparent seafloor outcrop of the BSR at 5110. Strong but discontinuous reflections immediately beneath the BSR between CMP 5417–5528 and CMP 5240–5390 and deeper within the section may also be related to fluid migration.

Prior to considering the effect of hydrostatic rather than lithostatic pressure on the derived phase diagram, we had tentatively interpreted the observations of Figure 6d to indicate a landward increase in heat flow of similar magnitude to that derived from BSR observations offshore Vancouver Island and modeled as being the result of sediment thickening and fluid expulsion [*Hyndman et al.*, 1993]. However, based on observations of near-hydrostatic pressures in the drill holes during leg 146 [*ODP Leg 146 Scientific Party*, 1993], we conclude that the hydrostatic pressure is the appropriate pressure to use for this calculation and that the data do not indicate any overall landward increase in heat flow.

In a study of pressure and temperature conditions at a BSR that was drilled in the Nankai trough, *Hyndman et al.* [1992] concluded that the in situ hydrate/free gas phase boundary was best decribed by the experimental phase boundary for methane in fresh water. Although our results suggest that the phase boundary for a saline solution similar to seawater is more appropriate, the data in Figure 6e could also be interpreted to indicate a slight landward increase in thermal gradient (and consequently heat flow) from about 0.055 °K/m to about 0.065 °K/m, assuming the freshwater stability curve.

Additional information on the nature of the BSR is contained in the wavelet shape (Figure 7) and in the large variations in amplitude of the BSR along the profile (Plate 1a). Whether amplitude variations in BSRs are due primarily to variations in the amount of gas hydrate within the sediment above the BSR or to variations in the amount of underlying free gas has been the subject of several recent papers [e.g., *Hyndman and Spence*, 1992; *Bangs et al.*, 1993; *Katzman et al.*, 1994; *Wood et al.*, 1994]. Along our profile, the wavelet shape associated with the BSR and recorded at near-vertical offset is consistently very simple and closely resembles a mirror image of the seafloor reflection, indicating that the impedance constrast generating this reflection is quite sharp relative to the wavelength of the seismic data and that if discrete layers of free gas or hydrate are present, they must either be very thin or have gradational upper (hydrate) and lower (gas) boundaries. Figure 7 also illustrates variability in the amplitude-versus-offset behavior of the BSR reflection.

As a first attempt to quantify these observations, we measured the amplitude ratio between the BSR and the seafloor reflection (Figure 8a) in order to derive limits on the reflection coefficient

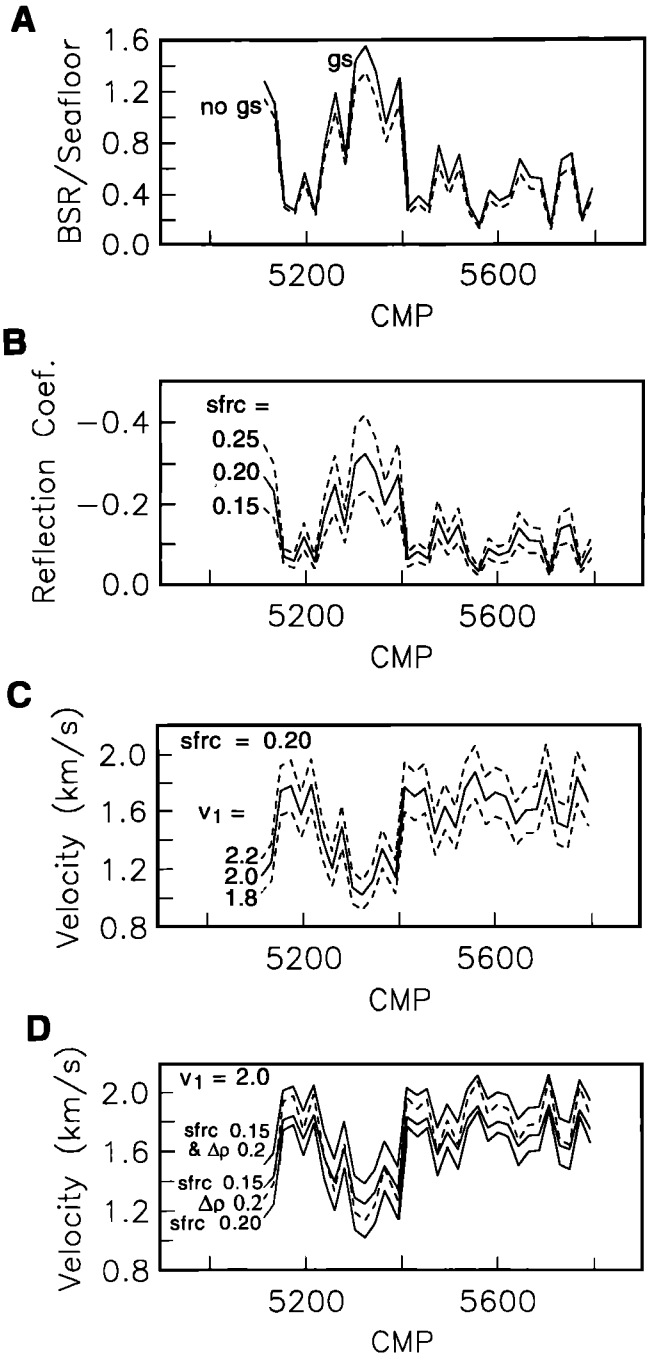

Figure 8. (a) Ratio of the peak-to-peak amplitude of the BSR to the amplitude of the seafloor reflection measured from raw data traces (curve labeled "no gs"). The effect of correcting for geometrical spreading (curved labeled "gs") is also shown, assuming velocities of 1.5 and 1.8 km/s for calculating path length in the water and sediments, respectively. (b) The reflection coefficient at the BSR derived from the amplitude ratios corrected for geometrical spreading assuming several different values for the seafloor reflection coefficient (sfrc). The effect of attenuation has not been included but may be quite large, especially for CMPs greater than 5400. (c) Velocity beneath the BSR derived from the reflection coefficients, assuming a seafloor reflection coefficient of 0.2 and several different velocities for the sediments above the BSR (V_1). (d) Effect on predicted sub-BSR velocities of varying the seafloor reflection coefficient and including a density inversion ($\Delta\rho$) beneath the BSR.

at the BSR. Again, this estimate depends on many parameters in addition to observed amplitudes, including the seafloor reflection coefficient, geometrical spreading of the wavefront, source and receiver array directivity, intrinsic attenuation within the sediments, attenuation due to scattering at a rough surface, and focussing and defocussing of energy due to lateral velocity heterogeneity. We attempted to derive an estimate of the seafloor reflection coefficient from measurements of the amplitude ratio between the seafloor reflection and the first seafloor multiple as recorded at twice the offset of the direct arrival. These amplitudes were corrected assuming a spherical divergence correction proportional to travel time. Because the amplitude of the seafloor multiple was difficult to pick on individual traces because of its low amplitude and interference with other arrivals, our measurements show considerable scatter, but range between 0.16 and 0.22. A seafloor reflection coefficient of 0.2 was similarly derived by *Hyndman and Spence* [1992] in their study of the BSR offshore Vancouver.

Peak-to-peak amplitudes of the seafloor reflection and and BSR were picked from unprocessed near-trace data filtered for anti-aliasing before recording and resampling at 8 ms. The measured amplitudes were corrected for geometrical spreading proportional to path length assuming velocities of 1.5 and 1.8 km/s in the water and sediment. Observed amplitude ratios are shown in Figure 8a, with and without the geometrical spreading correction. Assuming vertical incidence and following *Claerbout* [1976], the reflection coefficient at the BSR is $A(1-c^2)$, where A is the pressure amplitude ratio between the BSR and the seafloor reflection and c is the seafloor reflection coefficient. Reflection coefficients for the BSR calculated for assumed seafloor reflection coefficients of 0.15, 0.20, and 0.25 are shown in Figure 8b. Because the water depths in this study and the source-receiver offset for the near trace of 258 m imply incident angles of less than 15° on the BSR, assuming vertical incidence and neglecting source and receiver array directivity are much smaller sources of uncertainty than uncertainty in the seafloor reflection coefficient. The maximum reflection coefficient is very dependent on the assumed seafloor reflection coefficient and ranges from 0.25 to 0.43.

Attenuation and geometrical focussing are poorly known processes that may also have a large effect on apparent reflection coefficients. That intrinsic attenuation in the sediments, which depends on wavelet frequency and path length, is important is indicated in Figures 7a and 7b, where the frequency of the BSR wavelet decreases as BSR depth increases. Quantifying the effects of attenuation on measurements of peak-to-peak amplitude and separating this effect from interference effects due to the characteristics of reflecting interfaces is difficult. For this study, we neglected attenuation and note that this implies that our reflection coefficients may be considerably underestimated and that the amount by which the reflection coefficients are underestimated increases as the BSR deepens.

In order to place constraints on velocities above and below the BSR that are compatible with the derived reflection coefficients, we calculated the sub-BSR velocity implied by a range of assumed values for velocity and density above the BSR. For these estimates, we used assumed velocities above the BSR that are higher than those indicated by the interval velocities because it is likely that the velocity within the sediments above the BSR increases with depth. Because of the absence of additional coherent reflections within these sediments that would permit more detailed interval velocity estimates, however, we do not have any independent confirmation of the velocity above the BSR. The results of these calculations are summarized in Figure 8c, which shows the effect of different velocities above the BSR assuming a constant seafloor reflection coefficient (0.2) and density (2.0 g/m^3), and Figure 8d, which illustrates the additional effect of varying the seafloor reflection coefficient and including a density inversion of 0.2 g/m^3 beneath the BSR. In Figure 8c, velocities lower than 1.2 km/s are obtained beneath the BSR between CMPs 5250 and 5400 for assumed velocities above the BSR that range from 1.8 to 2.2 km/s. Such velocities imply the presence of a few percent, by volume, of free gas in the sediments beneath the BSR [*Hyndman and Spence*, 1992; *Bangs et al.*, 1993; *MacKay et al.*, 1994]. Even if one considers the extreme case of a seafloor reflection coefficient of 0.15, a density decrease beneath the BSR from 2.0 to 1.8 g/m^3, and a velocity of 2.0 km/s above the BSR, a sub-BSR velocity lower than that of seawater is indicated. Although the apparent sub-BSR velocities west of CMP 5400 are considerably higher and do not require the presence of free gas, these estimates may be considerably underestimated because we have neglected the effect of attenuation, which may decrease the apparent reflection coefficient by as much as 40%. We conclude that the large amplitude of the BSR observed beneath the mid-slope region along this profile suggests the presence of methane, both in the form of free gas and gas hydrate, within the older parts of the accretionary complex offshore Oregon.

In an attempt to understand the origin of the methane, we looked deeper in the seismic section. Few coherent reflections are observed either above or just below the BSR. However, a locally strong but discontinuous reflective zone is observed 0.5 to 1.0 s beneath the BSR (Figure 4 and Plate 1a). The ocean bottom seismometer data indicate that the average velocity between this reflective "surface" and the seafloor is less than 2.0 km/s (Figure 4c), suggesting several explanations for this zone. One explanation is that it represents the base of a midslope basin formed either in situ or as a lower slope basin (similar to the one labeled LSB on Figure 4b) and subsequently tilted and uplifted. The absence of any coherent layered structure within this basin and its discontinuous nature, however, argue against this interpretation. We believe that this reflective zone may represent the base of a large debris flow. High-resolution topography from the region shows several arcuate ridges that are concave landward (AR on Plate 1b) and may represent the downslope signature of sediment instability over a large (approximately 15x20 km) region. The seismic reflection data also suggest that midslope sediments may overly the flat lying sediments of the lower slope basin between CMP 5910 and 6010, although this might also be an artifact of incomplete migration.

Exceptionally bright spots within this region (question marks on Plate 1a and Figure 7b), which show both normal and reversed polarity, may be reflections and diffractions from the top and/or bottom of diffuse pockets of free gas or overpressured fluids. We speculate that these fluids and/or gas migrate upward through the sediment column and are trapped beneath the BSR, where they migrate laterally until they are vented at the surface where the BSR outcrops on the seafloor and along small faults. A small circular hill observed about 0.5 km south of CMP 5350 (Plate 1b) may be a mud volcano, providing further evidence of active fluid movement (and density inversions) within the older part of the accretionary prism.

In an attempt to determine whether the midslope BSR we observe is a widespread feature of the upper slope or is genetically related to the apparent debris flow we have identified in the bathymetric data, we scanned the existing database in this region.

Very few seismic lines cross this part of the slope. A USGS multichannel seismic reflection profile that crosses the slope approximately 15 km north of our profile (approximately along the northern boundary of Plate 1b) does not show any sign of a BSR in this region. It is interesting to note that both the landslide and large fluid accumulations in this region may be related to the Daisy Bank fault, which passes along its southwestern edge (Figure 1). This fault may have contributed to slope instability either through shaking during an earthquake or by serving as a deep conduit for fluid transport. We further speculate that this process may contribute to the formation of headless canyons on the continental slope.

Because the BSR appears to crop out on the seafloor at a depth where it can be relatively easily sampled and observed, this site may be a good test site for studying BSR formation and evolution on active margins. A recent study of an exposed BSR at 540 m depth in the Gulf of Mexico has documented this process on a passive margin and shown that the formation and dissociation of gas hydrate is a significant factor in the trapping and release of oil and gas [*MacDonald et al.*, 1994]. Additional data, including seismic data to map the regional extent of the BSR and correlate it with topography and sampling of the heel and toe of the apparent slump, will also be needed to resolve the multiple uncertainties concerning origin and amount of methane hydrate and free gas in the older part of the accretionary complex and the possible relationship between methane and slope stability.

The Continental Shelf and Subduction Zone Backstop

A deep basin that records a complex history of changing depocenters, erosion, folding, faulting, and intrusion is found on the continental shelf. Seismic profiles from this region are well known as textbook examples of unconformities [e.g., *Sheriff and Geldart*, 1982]. The basement reflection beneath this basin (SB on Figure 4b) is shown in the migrated data to be a block-faulted surface, probably formed by normal faulting in an extensional regime soon after accretion of the Siletz terrane to North America [*Snavely et al.*, 1980]. Although such a structure was suggested by the earlier USGS data, the faulted character of this surface was poorly defined in those unmigrated data. The new data also more clearly define the seaward edge of the Siletz basement (labeled FF on Figure 4b). We note, however, the presence of several diffractions seaward of this boundary (D on Figure 4b), which may represent out-of-plane events resulting from possible along-strike variations in the westward extent of the Siletz block.

Beneath the basement reflection, a deep reflection is observed at about 8-s twtt. No reflections were observed beneath the Siletz basement in the earlier data, and the base of the crust was assumed to be at about 16 km beneath the shelf, based on an old refraction profile in the onshore Coast Range [*Berg et al.*, 1966]. Evidence that these reflections (labeled DCR on Figure 4b) are primary events from the lower crust was discussed above. In the absence of coincident large aperture data, one might be tempted to identify these events as the Moho, and the crustal thickness of about 16–18 km derived from such an interpretation would be consistent with the earlier refraction data and with subsequent estimates of crustal thickness derived from gravity modeling [*Couch and Riddihough*, 1989]. The large aperture data [*Tréhu et al.*, 1994], however, indicate that the base of the crust is dipping east in this region and is at a depth of 22 km near km 105 and 30 km near the coast (km 135). The twtt to the Moho predicted by the model derived from the large aperture data is shown on Figure 4c.

One explanation for these deep reflections is that they represent reflections from a velocity inversion underlying the base of the Siletz terrane. Alternatively, they may represent reflections from a velocity increase occurring at the top of the subducted oceanic crust (or, more likely, the top of lower oceanic crust, since the upper oceanic crust seems to have been significantly disrupted and incorporated into the accretionary prism); this explanation requires that a layer of sediment be sandwiched between the base of the Siletz terrane and the subducted oceanic crust in order to have lower-velocity material overlying the subducted crust of the Juan de Fuca plate. It is also possible that the observed reflection represents an interference pattern between reflections from the base of the Siletz and the top of oceanic crust. Because of the poor signal to noise ratio of this event, we did not attempt quantitative modeling of the waveform and polarity of this reflection. The uncertainty about whether it represents the base of the Siletz or the top of the subducted lower oceanic crust is important for evaluating models of upper plate/lower plate interaction in this region and will be discussed in detail elsewhere.

A zone of disrupted reflections immediately overlies the seaward edge of the Siletz block (labeled FF in Figure 4b). This region of the seismic section is shown at large scale in Figure 9 and suggests a two-stranded strike-slip fault with very little vertical offset. Figure 9 suggests that this fault may disrupt the seafloor, implying recent activity. That this feature of the data reflects a true disruption of the strata and is not an artifact of processing is supported by a look at the original shot gathers, which show disruption of refracted arrivals as this region is crossed. Figure 10 shows three reduced record sections of shot gathers. The first (top, Figure 10) illustrates the refracted arrival when both the shot and streamer are east of the disrupted zone, and the other two sections show shots west of the disrupted zone when the streamer crossed the disrupted zone. When source and receiver are both on the same side of the disrupted zone, the wavelet is impulsive and simple. As soon as the disrupted zone is crossed, the wavelet is complicated and its amplitude is small. No similar zones of disruption are observed further east.

Although it is impossible to identify the trend of this fault from a single crossing, and a search of the available seismic reflection data [*Goldfinger et al.*, 1992] for a continuation of this feature was inconclusive, it is tempting to associate this event with the Fulmar Fault, identified by *Snavely* [1987] on the basis of magnetic anomalies and interpreted to be a strike-slip fault that resulted in northward transport of a portion of the forearc during the early mid-Eocene. In Snavely's model [*Snavely*, 1987], the Fulmar Fault is a late-middle to early-late Eocene feature that resulted in truncation of the seaward edge of the Siletz terrane and juxtaposition of early Eocene melange with Siletz rocks. Our data suggest that northward transport of the accretionary prism relative to the rest of the forearc may be continuing. An alternative explanation for the fault observed in our data is local deformation associated with the anticline that overlies the seaward edge of the Siletz terrane.

In either case, that the eastern boundary of the Siletz block is overlain by an active fault supports the suggestion of *Tréhu et al.* [1994] that this boundary plays a major role in localizing decoupling of the accretionary prism from the rest of the forearc. Decoupling between the western and eastern portion of the Cascadia forearc must occur somewhere beneath the continental shelf or Oregon Coast Range because the offshore left lateral stike-slip faults of *Goldfinger et al.* [1992] indicate a stress regime where the major axis of compression is directed approxi-

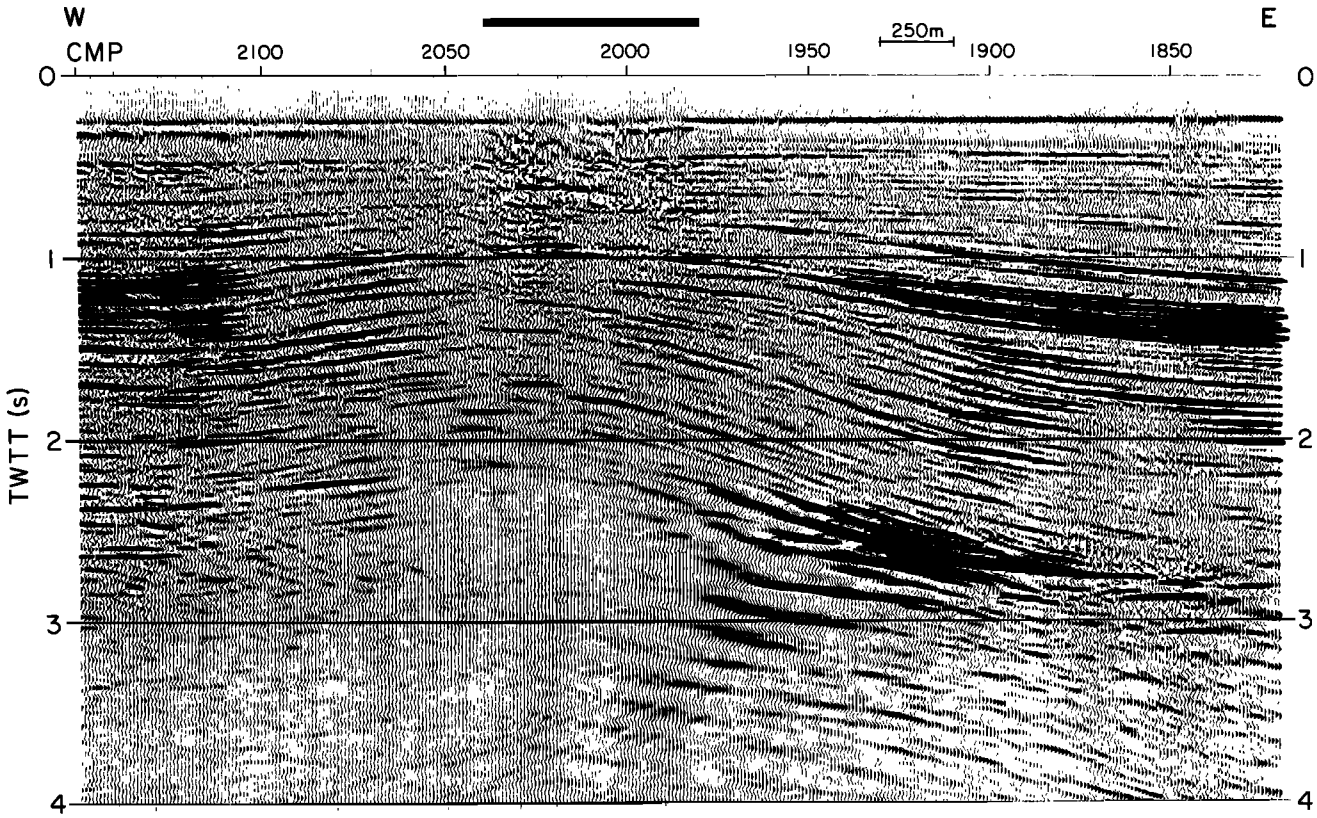

Figure 9. Detail of the seaward edge of Siletz basement and disruptions in the overlying sediments. The horizontal black bar at the top of the figure indicates the region interpreted to be a recent strike-slip fault zone, which is tentatively interpreted to be a modern manifestation of the Fulmar Fault of *Snavely et al.* [1980; *Snavely*, 1987].

mately east-west, whereas onshore data from the Willamette Valley indicate north-south directed compression [*Werner et al.*, 1991, 1992; *Madin et al.*, 1993]. Other evidence of the influence of Siletz terrane crustal stucture on forearc deformation that is cited by *Tréhu et al.* [1994] includes large along-strike variations in the width of the postaccretion subduction complex and in forearc seismicity that are correlated with along-strike variations in the thickness of the Siletz terrane and in backstop geometry.

Conclusions

Several new constraints on the crustal structure of the Cascadia subduction zone and on methane within the accretionary prism have been obtained from a deep crustal seismic reflection profile that was collected as part of a comprehensive onshore/offshore seismic imaging experiment across the continental margin. These constraints are summarized in Figure 11 and include the following.

1. Recognition of a deep reflection beneath the continental shelf. That this reflection must come from within the crust rather than from the Moho is required by coincident large aperture data. The reflection may indicate either the base of the accreted Siletz terrane, the top of the subducted lower oceanic crust, or an interference pattern between reflections from both of these boundaries. This interpretation suggests that the interpretation of similar deep reflections from regions where no coincident large aperture data are available is uncertain.

2. Identification of a shallow, recently active fault that disrupts a 0.75-km-wide region and shows little vertical displacement. This fault overlies the seaward edge of the Siletz terrane and suggests that the accretionary prism seaward of the Siletz terrane may be at least partially decoupled from the rest of the forearc. Recent submersible observation of a carbonate chimney in this fault zone suggests that this fault zone may also be associated with fluid flow in the forearc (R. Yeats, personal communication, 1994).

3. Observation of a very strong BSR beneath the midslope region 25–35 km landward of the deformation front. The inferred temperature and pressure at the BSR is consistent with the experimentally determined phase diagram for a methane/seawater phase diagram over a wide range of temperatures and pressures if one assumes hydrostatic pressure and the temperature gradient measured at the base of the slope during ODP leg 146. This result provides strong confirmation of the generally accepted hypothesis that BSRs are associated with the base of the methane hydrate stability zone. Although using BSR observations as a proxy for heat flow is subject to several uncertainties, the data suggest that heat flow through the midslope region is relatively uniform, except for localized zones of higher apparent heat flow related to a small fault and to where the BSR appears to outcrop on the seafloor. Approximate reflection coefficients derived from the data suggest the presence of a small amount of methane hydrate overlying the BSR and of free gas below it, consistent with results from ODP leg 146. Multiple uncertainties prevent a precise estimate of the relative volumes of gas and hydrate, but interval velocities of only 1.5–1.7 for the overlying layer indicate that the amount of hydrate is relatively low. It cannot be determined from the limited number of existing seismic profiles across

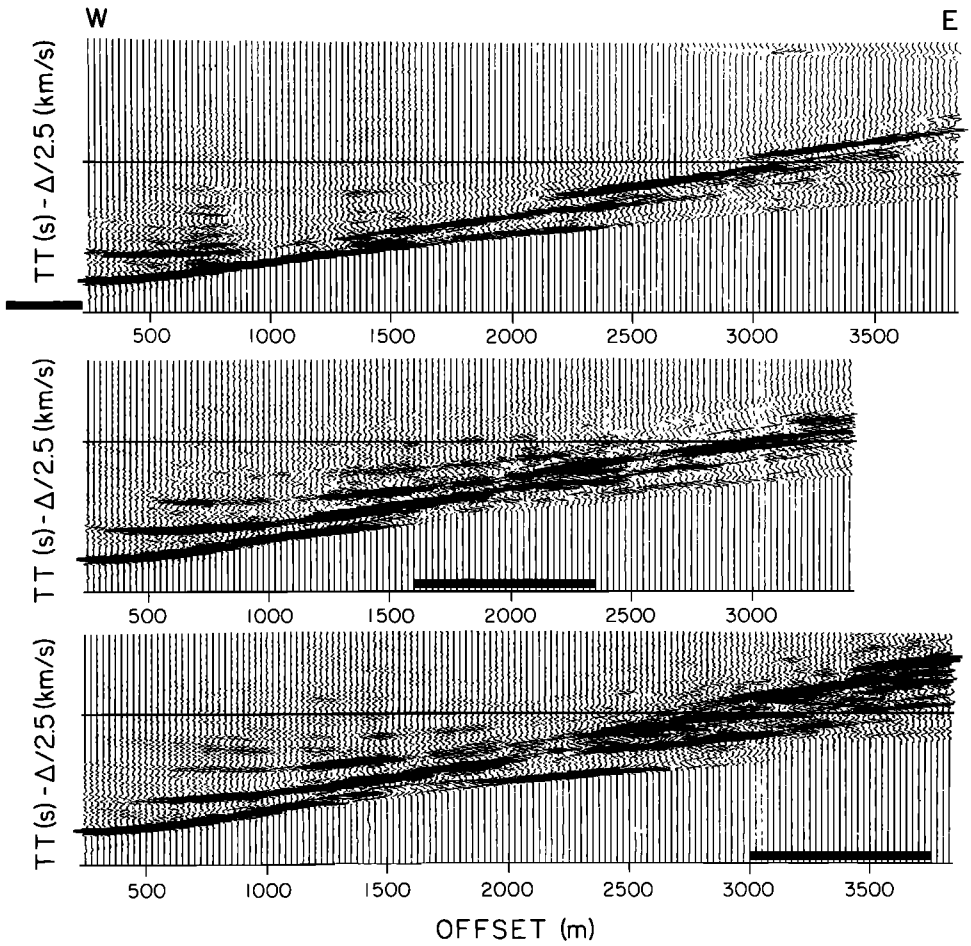

Figure 10. Record sections of shot gathers as the ship traveled from east to west across the disrupted zone tentatively interpreted to be the Fulmar Fault. The horizontal black bar parallel to the offset axis indicates the location of the fault zone similarly marked on Figure 9.

the continental slope whether the apparent presence of free gas and gas hydrate in this part of the accretionary complex is genetically related to slope instability that has been inferred on the basis of the new seismic data and high-resolution regional bathymetry and/or to the Daisy Bank fault, which is a northwest trending left-lateral strike-slip fault that extends from the abyssal plain to the continental shelf and crosses the slope approximately 15 km south our seismic profile.

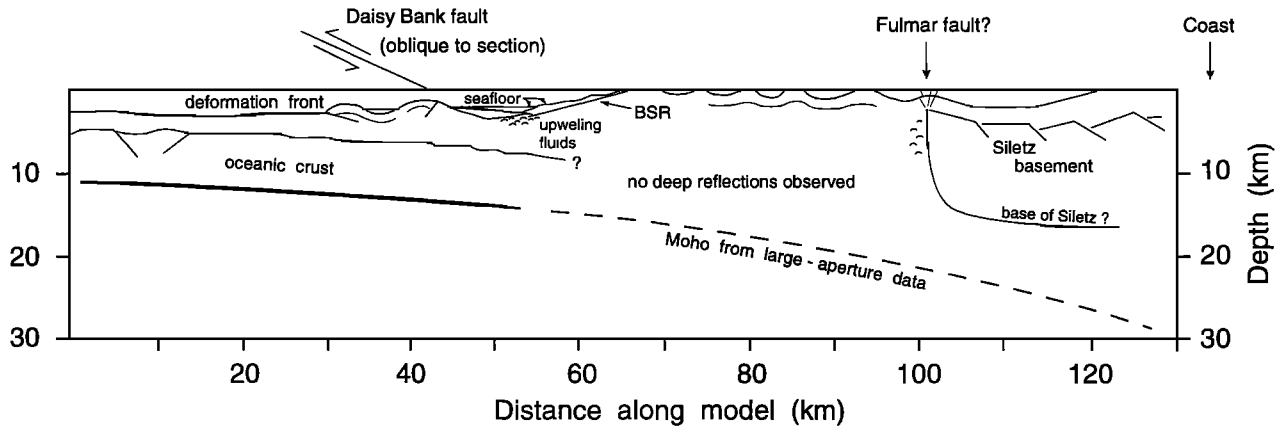

Figure 11. Schematic summary of constraints on methane distribution and crustal structure on the Oregon continental margin obtained from the seismic reflection profile discussed in this paper.

Acknowledgments. Many people assisted in the acquisition and processing of these data. Vern Kulm, Greg Moore, and Casey Moore encouraged this piggyback experiment on their high-resolution seismic survey, which was conducted as a site survey for the Ocean Drilling Program. Guy Cochrane spent the extra day at sea as the scientific observer on the R/V *Geotide* and made sure that data were properly recorded. Guy Cochrane and Mary MacKay processed the seaward portion of the profile as part of the ODP site survey. Jianing Shi and Tim Holt assisted in the early stages of data processing at OSU. Lili Weldon suggested that the midslope basin might be a landslide, inspiring us to look at the high-resolution topography for confimation. Discussions with Kristin Rohr led to a better appreciation of the uncertainties associated with estimation of reflection coefficients. Nathan Bangs and an anonymous reviewer provided insightful and constructive reviews of the manuscript. Acquisition and analysis of these data was supported by the National Science Foundation through grant OCE-8900963. Related work on the coincident velocity model was supported by grant EAR-8905189 and USGS grant 14-08-0001-G2072.

References

Applegate, B., M. Mackay, L.D. Kulm, C.G. Fox, R.W. Embley, and P.J. Meis, A left-lateral strike-slip fault seaward of the central Oregon convergent margin, *Tectonics*, *11*, 465–477, 1992.

Atwater, B.F., Evidence for great Holocene earthquakes along the outer coast of Washington State, *Science*, *236*, 942–944, 1987.

Bangs, N.L.B., D.S. Sawyer, and X. Golovchenko, Free gas at the base of the gas hydrate zone in the vicinity of the Chile triple junction, *Geology*, *21*, 905–908, 1993.

Berg, J.W., Jr., et al., Crustal refraction profile, Oregon Coast Range, *Seismol. Soc. Am. Bull.*, *56*, 1357–1362, 1966.

Brocher, T.M., M.J. Moses, and A.M. Tréhu, Onshore-offshore wide-angle seismic recordings from central Oregon: Five-day recorder data, *U. S. Geol. Surv. Open File Rep.*, *93-318*, 24 pp., 1993.

Claerbout, J. F., *Fundamentals of Geophysical Data Processing*, 274 pp., Blackwell Scientific, Cambridge, Mass., 1976.

Cochrane, G. R., J.C. Moore, M.E. MacKay, and G.F. Moore, Velocity and inferred porosity model of the Oregon accretionary prism from multichannel seismic reflection data: Implications on sediment dewatering and overpressure, *J. Geophys. Res.*, 99, 7033–7044, 1994.

Couch, R.W., and R.P. Riddihough, The crustal structure of the western continental margin of North America, in Geophysical Framework of the Continental United States, edited by L.C. Pakiser and W.D. Mooney, *Geol. Soc. Am. Mem.*, *172*, 103–128, 1989.

Davis, E.E., R.D. Hyndman, and H. Villinger, Rates of fluid expulsion across the northern Cascadia accretionary prism: Constraints from new heat flow and multichannel seismic reflection data, *J. Geophys. Res.*, *95*, 8869–8889, 1990.

Goldfinger, C., L.D. Kulm, R.S. Yeats, B. Applegate, M.E. MacKay, and G.F. Moore, Transverse structural trends along the Oregon convergent margin: Implications for Cascadia earthquake potential and crustal rotations, *Geology*, *20*, 141–144, 1992.

Grant, W.C., B.F. Atwater, G.A. Carver, M.E. Darienzo, A.R. Nelson, C.D. Peterson, and G.S. Vick, Radiocarbon dating of late Holocene coastal subsidence above the Cascadia subduction zone—Compilation for Washington, Oregon and northern California, *Eos Trans. AGU*, *70*, 1331, 1989.

Heaton, T.H., and S.H. Hartzell, Earthquake hazards on the Cascadia subduction zone, *Science*, *236*, 162–168, 1987.

Hyndman, R.D., and E. E. Davis, A mechanism for the formation of methane hydrate and seafloor bottom-simulating reflectors by vertical fluid expulsion, *J. Geophys. Res.*, 97, 7025–7041, 1992.

Hyndman, R.D., and G.D. Spence, A seismic study of methane hydrate marine bottom simulating reflectors, *J. Geophys. Res.*, 97, 6683–6698, 1992.

Hyndman, R.D., J.P. Foucher, M. Yamano, A. Fisher, and Scientific Team of Ocean Drilling Program leg 131, Deep sea bottom-simulating-reflectors: Calibration of the base of the hydrate stability field as used for heat flow estimates, *Earth Planet. Sci. Lett.*, *109*, 289–301, 1992.

Hyndman, R.D., K. Wang, T. Yuan, and G.D. Spence, Tectonic sediment thickening, fluid expulsion, and the thermal regime of subduction zone accretionary prisms: The Cascadia margin offshore Vancouver Island, *J. Geophys. Res.*, 98, 21,865–21,876, 1993.

Katzman, R., W.S. Holbrook, and C.K. Paull, Combined vertical-incidence and wide-angle seismic study of a gas hydrate zone, Blake Ridge, *J. Geophys. Res.*, *99*, 17,975–17,996, 1994.

Kulm, L.D., et al., Oregon subduction zone: Venting, fauna and carbonates, *Science*, *231*, 561–566, 1986.

Lewis, B.T.R., Changes in P and S velocities caused by subduction related sediment accretion of Washington/Oregon, in *Shear Waves in Marine Sediments*, edited by J. Kloven and R. Stoll, pp. 379–386, Kluwer Academic, Norwell, Mass., 1992.

MacDonald, I.R., N.L. Guinasso Jr., R. Sassen, J.M. Brooks, L. Lee, and K.T. Scott, Gas hydrate that breaches the sea floor on the continental slope of the Gulf of Mexico, *Geology*, *22*, 699–702, 1994.

MacKay, M.E., G.F. Moore, G.R. Cochrane, J.C. Moore, and L.D. Kulm, Landward vergence and oblique structural trends in the Oregon margin accretionary prism: Implications for fluid flow, *Earth Planet. Sci. Lett.*, *109*, 477–491, 1992.

MacKay, M.E., R.D. Jarrad, G.K. Westbrook, R.D. Hyndman, and the Shipboard Scientific Party of ODP leg 146, Origin of bottom simulating reflectors: geophysical evidence from the Cascadia accretionary prism,*Geology*, *22*, 459–462, 1994.

Madin, I.P., G.R. Priest, M.A. Mabey, S. Malone, T.S. Yedlin, and D. Meier, March 25, 1993, Scotts Mills earthquake—western Oregon's wake-up call, *Oreg. Geol.*, *55*, 51–57, 1993.

Moore, J.C., D. Orange, and L.D. Kulm, Interrelationship of fluid venting and structural evolution: Oregon margin, *J. Geophys. Res.*, *95*, 8795–8808, 1990.

Moore, J.C., K.M. Brown, F. Horath, G. Cochrane, M. MacKay, and G. Moore, Plumbing accretionary prisms: Effects of permeability variations, *Proc. R. Soc. London*, *335*, 275–288, 1991.

ODP Leg 146 Scientific Party, ODP leg 146 examines fluid flow in Cascadia margin, *Eos Trans. AGU*, *74*, 345–347, 1993.

Shedlock, K.M., and C.S. Weaver, Program for earthquake hazards assessment in the Pacific Northwest, *U.S. Geol. Surv. Circ. 1067*, 29 pp., 1991.

Sheriff, R.E., and L.P. Geldart, *Exploration Seismology, vol. 2 Data Processing and Interpretation*, 221 pp., Cambridge University Press, New York, 1982.

Shipley, T.H., M.H. Houston, R.T. Buffler, F.J. Shaub. K.J. McMillen, J.W. Ladd, and J.L. Worzel, Seismic evidence for widespread possible gas hydrate horizons on continental slopes and rises, *Am. Assoc. Pet. Geol. Bull.*, *63*, 2204–2213, 1979.

Snavely, P.D., Jr., Tertiary geologic framework, neotectonics, and petroleum potential of the Oregon-Washington continental margin, in *Geology and Resource Potential of the Continental Margin of Western North America and Adjacent Ocean Basins—Beaufort Sea to Baja California*, *Earth Sci. Ser.*, vol. 6, edited by D.W. Scholl, A. Grantz, and J.G. Vedder, pp. 305–335, Circum-Pacific Council for Energy and Mineral Resources, Houston, Tex., 1987.

Snavely, P.D., Jr., H.C. Wagner, and D.L. Lander, Geologic cross section of the central Oregon continental margin, *Geol. Soc. Am. Map Chart Ser.*, *MC-28J*, 1980.

Tobin, H.J., J.C. Moore, M.E. MacKay, D.L. Orange, and L.D. Kulm, Fluid flow along a strike slip fault at the toe of the Oregon accretionary prism: Implications for the geometry of frontal accretion, *Bull. Geol. Soc. Am.*, *105*, 569–582, 1993.

Tréhu, A. M., and Y. Nakamura, Onshore-offshore wide-angle seismic recordings from central Oregon: Ocean bottom seismometer data, *U.S. Geol. Surv. Open File Rep.*, *93-317*, 30 pp., 1993.

Tréhu, A.M., I. Asudeh, T. Brocher, J. Luetgert, W. Mooney, J. Nabelek, and Y. Nakamura, Crustal architecture of the Cascadia forearc, *Science*, *265*, 237–243, 1994.

Werner, K.S., E.P. Graven, T.A. Berkman, and M.J. Parker, Direction of maximum horizontal compression in northwestern Oregon determined by borehole breakouts, *Tectonics*, *10*, 948–958, 1991.

Werner, K.S., J. L. Nabelek, R. Yeats, and S. Malone, The Mount Angel fault: Implications of seismic-reflection data and the Woodburn, Oregon, earthquake sequence of August 1990, *Oreg. Geol.*, *54*, 112–117, 1992.

Wood, W.T., P.L. Stoffa, and T.H. Shipley, Quantitative detection of methane hydrate through high-resolution seismic velocity analysis, *J. Geophys. Res.*, *99*, 9681–9695, 1994.

Yamano, M., S. Uyeda, Y. Aoki, and T.H. Shipley, Estimates of heat flow derived from gas hydrates, *Geology*, *10*, 339–343, 1982.

Zwart , G., and J.C. Moore, Variations in temperature gradient of the Oregon accretionary prism, *Eos Trans. AGU*, *74*(43), Fall Meeting suppl., 369, 1993.

C. Goldfinger, G. Lin, E. Maxwell, and A. M. Tréhu, College of Oceanic and Atmospheric Sciences, Oregon State University, Ocean Administration Building 104, Corvallis, OR 97331-5503. (e-mail: trehu@oce.orst.edu)

(Received May 17, 1994; revised January 20, 1995;
accepted January 20, 1995.)